Estimating wide-angle, spatially varying reflectance using time-resolved inversion of backscattered light

Nikhil Naik,[1] Christopher Barsi,[1,*] Andreas Velten,[1,2] and Ramesh Raskar[1]

[1]*Media Lab, Massachusetts Institute of Technology, 77 Massachusetts Ave., Cambridge, Massachusetts 02139, USA*
[2]*Morgridge Institute for Research, University of Wisconsin Madison, Madison, Wisconsin 53715, USA*
**Corresponding author: cbarsi@mit.edu*

Received February 7, 2014; accepted March 1, 2014;
posted March 14, 2014 (Doc. ID 206007); published April 8, 2014

Imaging through complex media is a well-known challenge, as scattering distorts a signal and invalidates imaging equations. For coherent imaging, the input field can be reconstructed using phase conjugation or knowledge of the complex transmission matrix. However, for incoherent light, wave interference methods are limited to small viewing angles. On the other hand, time-resolved methods do not rely on signal or object phase correlations, making them suitable for reconstructing wide-angle, larger-scale objects. Previously, a time-resolved technique was demonstrated for uniformly reflecting objects. Here, we generalize the technique to reconstruct the spatially varying reflectance of shapes hidden by angle-dependent diffuse layers. The technique is a noninvasive method of imaging three-dimensional objects without relying on coherence. For a given diffuser, ultrafast measurements are used in a convex optimization program to reconstruct a wide-angle, three-dimensional reflectance function. The method has potential use for biological imaging and material characterization.

OCIS codes: (110.3010) Image reconstruction techniques; (170.6920) Time-resolved imaging; (290.0290) Scattering.

http://dx.doi.org/10.1364/JOSAA.31.000957

1. INTRODUCTION

Optical signal transmission through random media has many applications, including deep-tissue imaging, underwater navigation, and atmospheric sensing. Because the wave equation is reversible, for coherent imaging, measurement of the complex field can be integrated with a spatial light modulator (SLM) to correct for strong scattering. This is the principle behind digital phase conjugation, in which a phase-conjugated signal propagates backward through a complex medium to produce an image [1]. Unfortunately, these methods typically rely on double passage through the material, embedded markers [2], or multimodal coupling [3–5]. Alternately, knowledge of the medium's transmission matrix [6,7] can allow for image reconstruction numerically or for prepatterning an image before propagation through the medium to mitigate multiple scattering and produce a focal spot [8–10]. These methods, however, still rely on coherence and begin to break down when the signal bandwidth is larger than D^2/L [11], where D is the material's diffusion constant and L is the sample thickness. Therefore, they are less effective for applications with temporally incoherent or wideband sources [12–14]. Because of this limitation, generalization to fluorescent imaging or white light has been limited to small angles of view via the memory effect [15,16], precluding imaging objects larger than a few millimeters. It has been suggested that correlation-based methods are unsuitable for large-scale imaging, such as mappings to turbulent environments [17].

By exploiting the time behavior of scattered light instead, we do not suffer from these restrictions. In particular, we reconstruct an unknown spatially varying reflectance with a large angle of view compared to correlation or interference methods, whose typical scale is a few wavelengths. The key insight comes from recognizing that time resolution is useful for more than rejecting scattered light, as is done in traditional time-resolved imaging modalities such as lidar [18], gated viewing [19], and optical coherence tomography [20].

Time delays of scattered light are naturally coupled to spatial frequencies [21,22]. Therefore, per-pixel time profiles of scattered light contain useful information about the object. Indeed, it was shown recently that the time profile of light, having undergone multiple scattering, can be used to reconstruct three-dimensional geometries hidden from view [23,24]. Whereas this previous work focused on ideal diffusers and uniform reflectors, we generalize the method here to account for spatially varying reflectance, which is important for measuring, e.g., contrast agents in clinical imaging.

2. METHODS

The experimental setup is shown in Fig. 1. A pulsed laser source of intensity I_0 is focused onto a ground glass diffuser at point x_l. Light scatters through the diffuser toward a three-dimensional object (consisting of discrete points in Fig. 1), which has a spatially varying reflectance $R(x)$. Light is scattered by an object point back through the diffuser, where it is finally imaged onto a streak camera with a 2 ps time resolution. Laser scanning compensates the 1D field of view of the camera by modeling different viewpoints [25] for a fixed camera position.

Our light source is a mode-locked 795 nm Ti:sapphire laser with pulses of approximately 50 fs in duration at a repetition

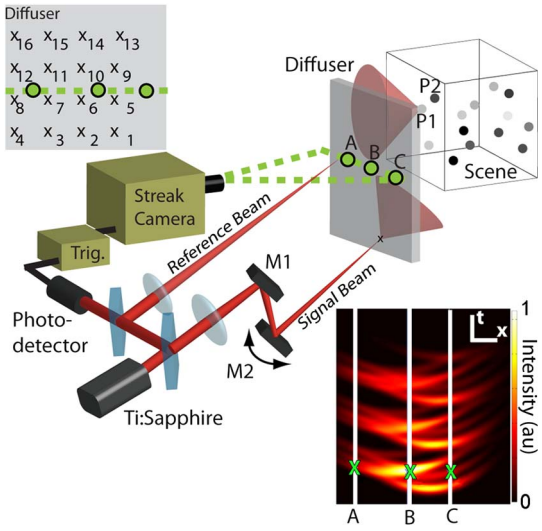

Fig. 1. Experimental setup. Pulses from a Ti:sapphire laser are focused onto a ground glass diffuser. The scattered light strikes a three-dimensional scene (here, a collection of point objects P_j) and is scattered back through the diffuser, which is imaged onto a streak camera. A streak image is recorded for 16 different laser positions incident on the diffuser (top left inset). The streak camera has a one-dimensional aperture and records the time profile of a horizontal line (dotted green line) of the diffuser. Bottom right inset: a simulated streak image for the point cluster. Sample pixels A, B, and C record the time profile of every P_j at those positions. Scale: 20 mm (horizontal), 100 ps (vertical).

rate of 75 MHz. A lens focuses this beam onto a ground glass diffuser (Edmund Optics, 120 grit). The incident laser spot is scanned across the diffuser with a pair of galvo-actuated mirrors. The detector is a Hamamatsu C5680 streak camera that captures a space-time (x–t) image of 672×512 pixels. The camera's nominal time resolution is 2 ps. The integration time for a streak image (one for each laser position) is 10 s to obtain sufficient SNR.

A portion of the beam is split and focused onto the diffuser directly in the line of view of the camera. This acts as a calibration spot to account for systematic fluctuations (laser intensity fluctuation and timing jitter) during acquisition. Images are normalized by the peak intensity of this calibration spot, and the time bins in each streak image (corresponding to a different incident laser position) are shifted so that the calibration spot in each image is centered at the same location.

Theoretically, in the geometric approximation [23] with no occlusions, the time-resolved streak image $I_l(x,t)$ for a given incident laser position x_l is

$$I_l(x,t) = I_0 \int g(x_l,x,x')R(x')\delta(ct-(r_l(x')+r_c(x')))\mathrm{d}x', \quad (1)$$

where $r_l(x') \equiv \|x_l - x'\|$ and $r_c(x') \equiv \|x' - x\|$ are the (time-independent) distances from laser point x_l to object point x' and from x' to diffuser point x, respectively. The delta function restricts the integrand to those light paths that reach the detector at time t. Thus, $I_l(x,t)$ is a weighted integral of $R(x')$ over the curve $\|x_l - x'\| + \|x' - x\| = ct$, i.e., Eq. (1) represents a tomography problem with a baseline limited by the diffuser area. Here, $g(x_l,x,x')$ is a physical weighting factor that depends on only the scene geometry and diffuser properties:

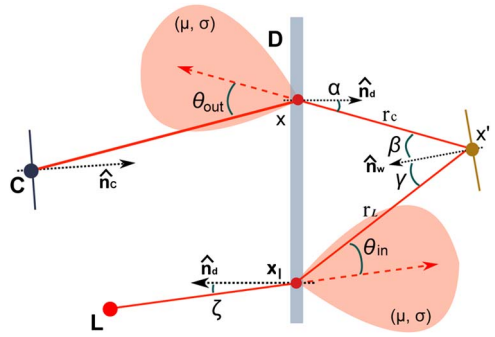

Fig. 2. Ray optics model for simulating image formation. The model uses the angles and distances of the relevant scene for each object point x'.

$$g(x_l,x,x') = \cos(\zeta(x_l))N(\theta_{\mathrm{in}}) \times \frac{\cos(\gamma(x'))\cos(\beta(x'))\cos(\alpha(x'))}{\pi^2 r_l^2(x') r_c^2(x')} N(\theta_{\mathrm{out}}), \quad (2)$$

where the angles α, β, γ, and ζ are due to contributions from the projected area of illumination, and $\theta_{\mathrm{in/out}} = \theta_{\mathrm{in/out}}(x_l,x,x')$ is the angle between the input/output ray and the diffuser normal (Fig. 2). $N(\cdot)$ is the averaged intensity profile emanating from the diffuser. For the ground glass diffuser considered here, it is Gaussian, $N(\theta) = \exp(-(\theta-\mu)^2/2\sigma^2)$, where σ is the divergence of the diffuse light and μ is an offset of the central beam direction due to manufacturing tolerances of the diffuser thickness.

In principle, from Eq. (1), there are two possible unknown functions: the scattering profile and the object reflectance function. Thus, the inverse problem that we address consists of measuring $I_l(x,t)$ for $l = 1,2,\ldots,L$ and reconstructing the unknown reflectance function $R(x')$ and scattering profile $N(\cdot)$. We solve a convex optimization problem (as described in Section 3.B) to minimize the error norm

$$\underset{R(x'),N(\cdot)}{\operatorname{argmin}} \frac{1}{L}\sum_{l=1}^{L} \|\hat{I}_l^{\mathrm{meas}} - \kappa_l \hat{I}_l^{\mathrm{num}}\|_2, \quad \text{for} \quad 0 \le R(x') \le 1. \quad (3)$$

In Eq. (3), L is the number of captured streak images, $\hat{I}_l^{\mathrm{meas}}$ is the vectorized measured streak image for incident laser position l, and $\hat{I}_l^{\mathrm{num}}$ is the vectorized form of the corresponding numerical image [calculated directly from Eq. (1)]. The value of L was chosen experimentally by comparing the robustness of the reconstruction due to noise and the total acquisition time. κ_l is an unknown gain factor, determined simultaneously during reconstruction, to account for second-order experimental effects, including variation of the beam profile for different incident positions and the tolerance of the diffuser thickness. Because the geometry can be estimated from the streak images using similar methods [23,24], we assume the geometry to be known throughout. (The influence of geometry errors on the reflectance recovery is discussed in Section 4.) Therefore, Eq. (3) represents a cost functional with the unknown functions $N(\cdot)$ and $R(x')$, contained implicitly in $\hat{I}_l^{\mathrm{num}}$, to be determined.

3. RESULTS

A. Reconstructing Diffuser Properties

To simplify the recovery, we first calibrate the algorithm using a known object, a small square patch (15×15 mm) of unity

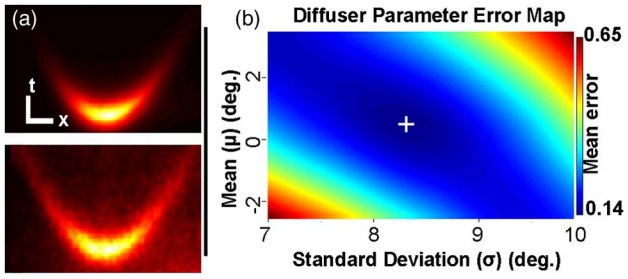

Fig. 3. (a) Top, experimentally measured streak image for a single incident laser position and single object point for a ground glass diffuser. Bottom, same as above with the ground glass diffuser replaced by a multiple scattering paper sheet. Scale bars: 100 ps, 20 mm. Color scale same as in Fig. 1 inset. (b) Error map showing the calculated optimal diffuser parameters. We use convex optimization to minimize the mean normalized l_2 error between simulation and captured data, and obtain the central direction (μ) and scattering width (σ) of the Gaussian. This error plot shows different errors for Gaussian parameters with the minimum marked by a white cross, for $\mu = 0.48°$ and $\sigma = 8.33°$, both comparable with the expected specifications.

reflectance, and treat only the diffuser parameters as unknowns in an iterative quadratic program. That is, we assume $R(x')$ is known but $N(\cdot)$ is unknown. For a single white object point at x_0, the reflectance reduces to a delta function, $R(x') \to \delta(x' - x_0)$, so that Eq. (1) becomes

$$I_l(x,t) \to I_0 g(x_l, x, x_0)\delta((ct - (r_l(x_0)) - r_c(x_0))). \quad (4)$$

The argument of the delta function implies that the impulse response of our time-resolved system is a hyperbola in the x–t plane. An example of a measured streak image for a given laser position is shown in Fig. 3(a). Increasing time corresponds to the vertical axis. Note that the intensity profile along the hyperbola is determined by g, which, for a known geometry, contains as unknowns the diffuser parameters μ and σ. Using these measured data, we recover optimal values of μ and σ via Eq. (3). The resulting error map, shown in Fig. 3(b), shows that these optimized values are $\mu = 0.48°$ and $\sigma = 8.33°$, which agree well with the values measured from the far-field intensity pattern. Other values of σ increase the mean normalized l_2 error (E) between forward rendering and actual data significantly, especially in the tails of the streak image, as shown in Fig. 4. The estimated parameters are then fixed for all future experiments. Thus, with a known input and measured output, we see that the statistical

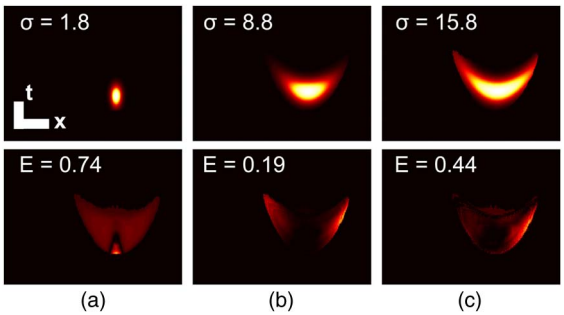

Fig. 4. Reconstruction errors in algorithm due to incorrect characterization of diffuser. Top row, reconstructed streak of a single white patch. Bottom row, error map for (a) $\sigma = 1.8°$, (b) $\sigma = 8.8°$, and (c) $\sigma = 15.8°$. Color scale same as in Fig. 1 inset.

properties of an unknown scattering material can be acquired, allowing for diffuser characterization and identification.

Although the results presented here use single scattering layers, the technique has potential for use in the multiple scattering regime. As an example, we replaced the ground glass with a sheet of paper, which has a thickness of 100 μm and a mean free path of 2 μm. We compared the measured streak image through paper and through the glass, and we find that the temporal blur is virtually the same [Fig. 3(a), bottom]. Indeed, this means that, for our given system, the time resolution is limited by the camera PSF (slit width, streaking blurring, aberrations, etc.) rather than by the diffuser itself. In contrast, the extension of using incoherent or broadband light to multiple scattering has been limited to thin layers [12,13]. The bandwidth limit in our case is purely a technological limit, whereas the correlation-based methods are inherently limited to (quasi) monochromaticity until wideband algorithms can be demonstrated.

B. Reconstructing Object Reflectance

With the diffuser properties known, we can estimate the unknown object reflectance as follows. Each measured streak image is vectorized by stacking the columns of the $N_x \times N_t$ image. The result is a set of L $(N_x N_t) \times 1$ vectors, labeled $\hat{I}_l^{\text{meas}}$ in Eq. (3). We then solve the constrained minimization problem in Eq. (3) using the interior point method and the *fmincon* solver from the MATLAB Optimization Toolbox. We provide a random initial guess for all unknown reflectances $R(x')$ with the constraint $0 \le R(x') \le 1$. The solver then finds the values of $R(x')$ that minimize the mean normalized l_2 error between the forward simulation [Eq. (1)] and the captured data. We terminate the optimization program either when the change in values of the objective function during a step is less than 10^{-15}, or when the difference between the reflectance function with its value in the previous step (i.e., $|R(x')_{i+1} - R(x')_i|$) is less than 10^{-15}. These constraints are provided to *fmincon* using the stopping criteria "TolFun" and "TolX," respectively. The convergence time of the optimization algorithm depends on the number of unknowns, the desired reconstruction accuracy (defined by the termination constraints), and quality of the random initial guess provided to the algorithm. For example, ~80 iterations are required for the scene in Fig. 8 given these termination constraints.

For the single layer case, other parametric models can be used for the diffuser, but the two parameters considered here are sufficient, as validated by two experiments (Fig. 5). First, with a single patch, we repeat the measurement with increasing angle θ of the patch normal with respect to the diffuser ($\cos\theta = \mathbf{n}_w \cdot \mathbf{n}_d$ in Fig. 2). The streak image is highly sensitive to such angular variation [Fig. 5(a)], with the mean percent error between numerical and measured intensity low and relatively constant up to a patch angle of 60° [Fig. 5(b)].

We next recover an unknown object, two frontoparallel patches of different reflectance values R_1 and R_2, to demonstrate wide field reconstruction. We keep the location of the first patch ($R_1 = 1$) fixed and shift the second patch ($R_2 = .7$) laterally. Both are located approximately 20 cm behind the diffuser. For a given incident laser position, there is significant change in the streak image [Fig. 6(a)], but the estimated reflectance R_2 is successfully recovered [Fig. 6(b)] for object

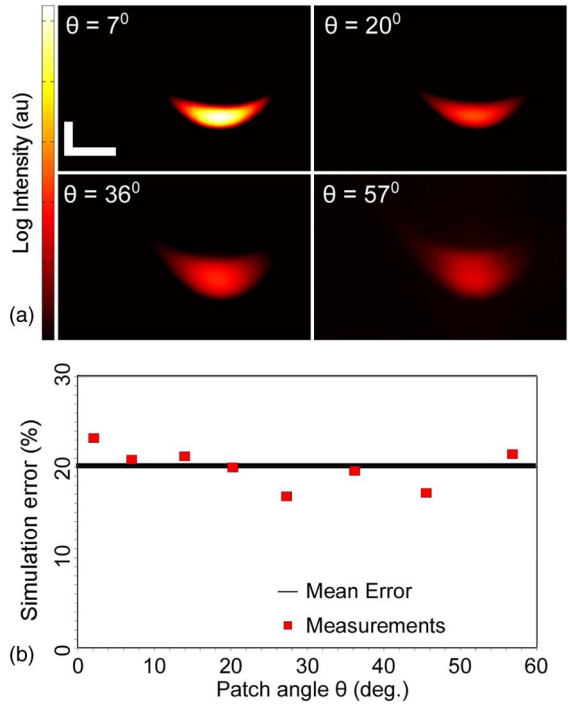

Fig. 5. Validation of model and reconstruction algorithm. (a) Streak data for single patch rotated at an increasing angle relative to the diffuser normal. Color scale same as in Fig. 1 inset. (b) Mean percent error between the captured data and forward simulation is low across a 60° range. Scale bars: 50 mm (horizontal), 200 ps (vertical).

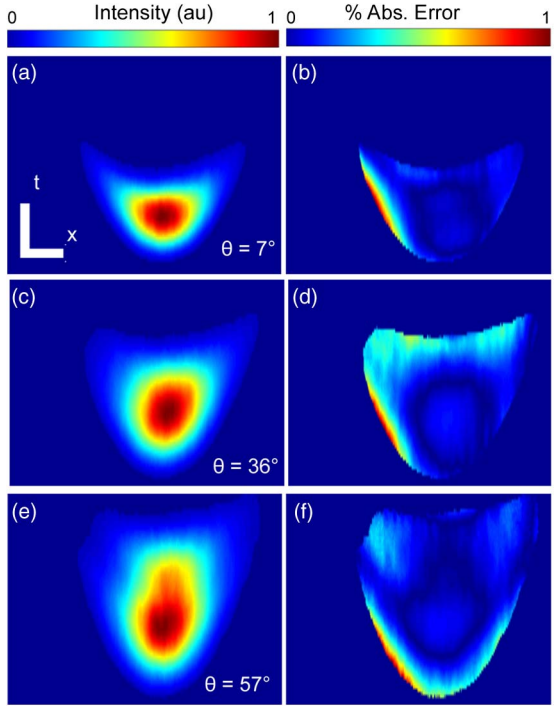

Fig. 7. Our geometric-optics-based model accurately simulates the streak image formation. The first column shows streak images captured for different θ using the configuration described in Fig. 4(a). The second column shows the pixel-wise percent error between the measured and computed intensity. Pixels with intensity below an absolute threshold (1% of maximum intensity) are set to zero, to avoid background noise. Scale bars: 25 mm (horizontal), 24 ps (vertical).

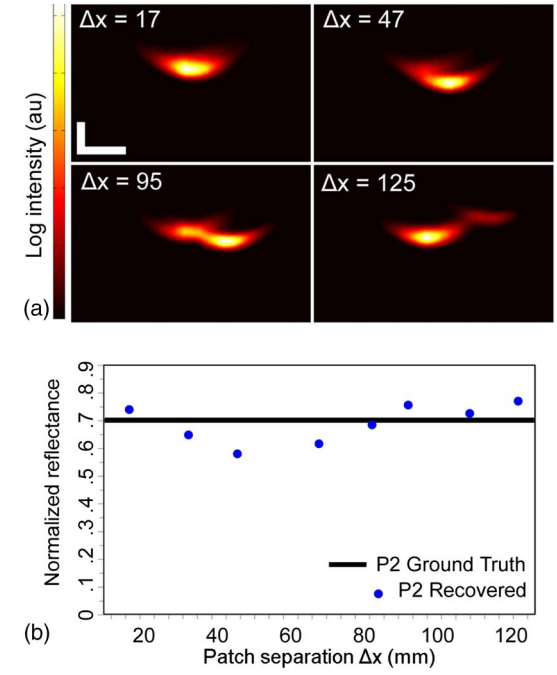

Fig. 6. Validation of model and reconstruction algorithm. (a) Streak data for two patches with increasing separation Δx (in mm). Color scale same as in Fig. 1 inset. (b) Reflectance is reconstructed successfully for separation up to 125 mm. The error in reflectance estimation is random and arises due to background noise and calibration errors. Scale bars: 50 mm (horizontal), 200 ps (vertical). Color map same as in Fig. 1 inset.

separations as low as 17 mm and as large as 125 mm, showing the method to be amenable for large angles of view.

We show further validation of our ray-optics-based model for image formation in Fig. 7. The mean absolute error between true and computed intensity of pixels is low (<20%) for high intensities, while it is much higher only for low intensities at the edges. This can be attributed to the high additive noise introduced by the camera during the integration process. The ray-optics-based model can calculate accurate values for high intensities robustly.

For more complex scenes, the streak image consists of a linear combination of hyperbolas from each object point P_i (Fig. 1, inset). In general, the system in not shift-invariant, with the curvature and the intensity profile of a given hyperbola changing with respect to object point locations. For well-separated points, it is relatively straightforward to reconstruct the scene, as individual hyperbolas themselves are separable (e.g., at green x's along pixels A and C in Fig. 1, inset). In general, however, this is not so and any given pixel can contain contributions from multiple points (at green x along B). Therefore, for a particular scene, there may not be enough pixels that record only a single contribution from each scene point to reliably recover the reflectance of all scene points. In such cases, it is not possible to recover the reflectance of all the scene points using only time-of-arrival information, as in gated imaging, making computational techniques necessary.

As an example, consider the scene in Fig. 8, a set of six patches that span a lateral field of 150 mm × 60 mm and a depth range of 13 mm. The convex optimization problem

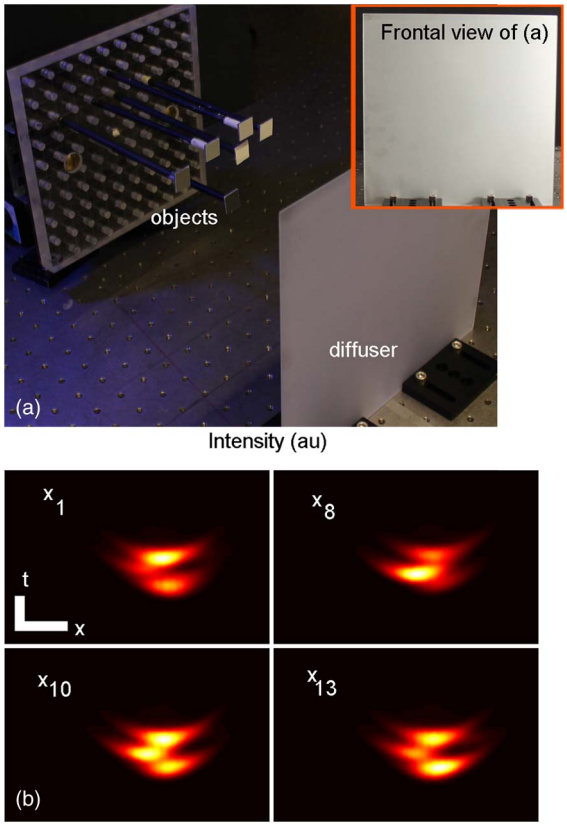

Fig. 8. Reconstruction of a complex scene. (a) Experimental setup of scene. (b) Streak data for four different incident laser positions (spatial configuration as seen in Fig. 1). Inset: frontal view of occluded scene with white light illumination. Occluded objects are not visible to the naked eye. Scale bars: 50 mm (horizontal), 200 ps (vertical). Color scale for (b) same as in Fig. 1 inset.

[Eq. (3)] allows for accurate reconstruction of all six patch reflectances, shown in Fig. 9. Note that, although there are six individual patches, only three individual streaks appear visible in the measured data [Fig. 8(b)], with the others "buried" in these dominant contributions. However, as shown in Fig. 9(b), we see that the reconstructed reflectances agree with the expected ones.

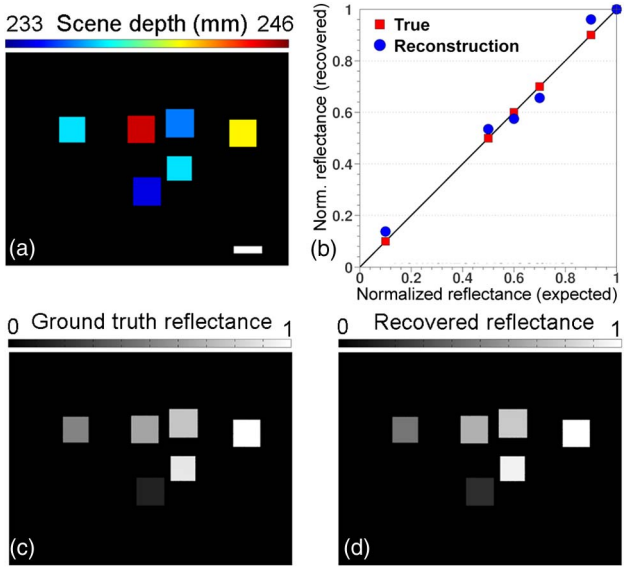

Fig. 9. Reconstruction of a complex scene. (a) Depth map of scene in Fig. 8, which is 110 mm wide with total depth variation 13 mm. (b) Comparison of reconstructed (blue circles) and ground truth (red squares) reflectances. (c) Ground truth and (d) reconstructed reflectance maps. Scale bars: 15 mm.

4. DISCUSSION

As noted previously, SLM-based methods are limited by the bandwidth of the source, whereas the time-resolved case presented here is limited by the bandwidth of the sensor as follows. Theoretically, we can expect the model to break down when the time T spent in the diffuser material exceeds the camera resolution T_c. Using the same dimensional analysis of the diffusion equation as in the coherent case, $T \sim L^2/D$. For a sample thickness of 100 μm, average refractive index of $n \sim 1.4$, and reduced scattering length of 10/cm, we calculate that $T \sim 100$ fs. This is $20\times$ less than the pixel resolution (2 ps) of the streak sensor, meaning that multiple scattering for biological samples of interest can be handled here. The incoherent method here has the advantage of not producing unwanted speckle in the measured and reconstructed images [26], which invariably occurs for transmission matrix methods [8].

For time-resolved imaging, the sensor's time resolution can decrease for nonideal conditions, including misfocus and aberrations. For the given setup here, robust reflectance recovery of centimeter-size scenes with depth variation on the order of millimeters requires a time resolution of $\delta t < 10$ ps. We demonstrate this by generating streak images (with 10% additive white Gaussian noise in intensity) for different time resolutions of $t = \{2, 20, 200$ ps$\}$ for the six-patch object from Fig. 8. We solve for scene reflectances using the same quadratic program and summarize the results in Fig. 10 and Table 1. This experiment also validates the robustness of our reconstruction algorithm to intensity noise.

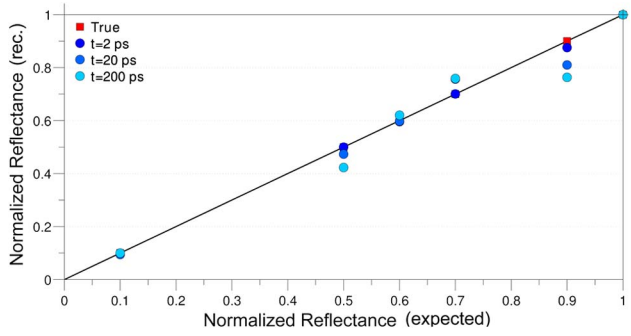

Fig. 10. Reflectance reconstruction for the scene in Fig. 8, simulating different time resolutions.

Table 1. Reflectance Reconstruction Using Time Resolutions in Fig. 10 Becomes Worse with Poorer Time Resolution

Patch Depth (mm)	239	246	235	237	238	243
True Reflectance	1	0.6	0.5	0.1	0.7	0.9
$t = 2$ ps	1	0.596	0.499	0.0982	0.7	0.875
$t = 20$ ps	1	0.597	0.473	0.0941	0.756	0.809
$t = 200$ ps	1	0.62	0.422	0.0999	0.758	0.763

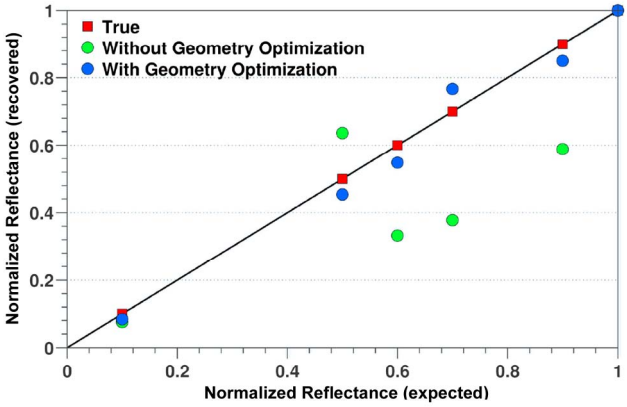

Fig. 11. Our approach is robust to small geometry errors. We can solve jointly for both reflectance and geometry to obtain accurate reconstruction given incorrect geometry.

Here, we have assumed the location of the unknown objects to be known. Our quadratic-program-based approach for reflectance reconstruction is robust to small errors in ground truth geometry. It is possible that the input geometry of the scene is not accurate if it is obtained using time-resolved reconstruction or due to other experimental errors. We simulate this case by introducing random errors in geometry. The reconstruction is poor if we solve for reflectance assuming the input geometry is correct. However, we can improve the reconstruction by solving a quadratic program jointly for both reflectance and geometry. The results are summarized in Fig. 11.

Further, we note that unknown patches can be accounted for by inputting into the algorithm more patches than expected. A spatially varying reflectance can, theoretically, include reflectance values of 0, which correspond to the absence of a patch. If no point is present at these locations, the reflectance value should be 0 (or comparable to the noise floor). For example, we simulate the expected streak images for the six-patch geometry shown in Fig. 8, but in the reconstruction algorithm, we assume there are ten unknown patch reflectances to recover. As shown in Fig. 12, the

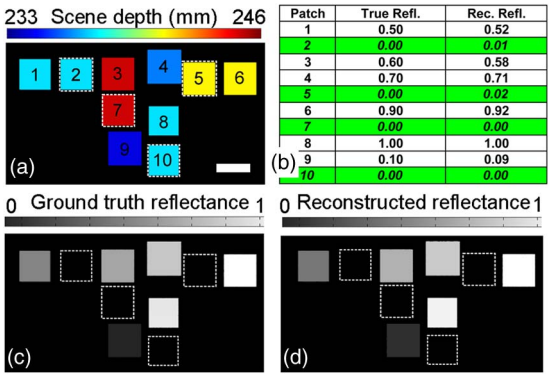

Patch	True Refl.	Rec. Refl.
1	0.50	0.52
2	*0.00*	*0.01*
3	0.60	0.58
4	0.70	0.71
5	*0.00*	*0.02*
6	0.90	0.92
7	*0.00*	*0.00*
8	1.00	1.00
9	0.10	0.09
10	*0.00*	*0.00*

Fig. 12. Our reconstruction algorithm is robust to the presence of additional erroneous patches. We correctly reconstruct the reflectance of six original patches, while solving for ten patches in total. (a) Depth map, with artificial patches highlighted with a dotted square. (c) and (d) are the ground truth and recovered reflectance values. Scale bar: 15 mm. (b) Corresponding reconstructed reflectance values. Note that artificial patches reconstruct a reflectance value of zero.

erroneous four patch locations yield a negligible reflectance for each. Thus, the presence or absence of an object (i.e., the shape) can be recovered at a given depth. The full generalization, to an unknown 3D shape and reflectance, can be completed through, e.g., sparsity-based methods [27], in which each unknown patch is parameterized by three spatial coordinates and one reflectance value. This is the subject of future work.

Conceptually, there is a much wider range of feature sizes that can be reconstructed. On one hand, the algorithm can be modified to include diffractive effects and is robust to small geometry measurement errors, making it amenable for extensions to smaller objects. On the other hand, because we rely on time resolution (Δt), larger features (Δz) are easier to identify ($\Delta z \sim c\Delta t$). Experiments would scale up using higher-power lasers and a wider camera aperture, as the measured intensity scales as the aperture divided by distance squared.

However, for biological applications, care must be taken not to damage the samples. The main limitation of the system is not time resolution, but dynamic range and noise, which worsens with multiple scattering. For this reason, the use of a microchannel plate (MCP) for gain is imperative. We expect that positive results can be obtained using similar power levels as found in time-resolved diffuse optical tomography [28], though recent nonlinear extensions to imaging suggest that stochastic resonance effects can enhance the signal using the noise energy [29].

With the discrete objects and scattering layer considered here, we expect that the method will become highly useful for imaging point-like sources via photoswitchable fluorophores for super- resolution [30,31], high-speed particle flow imaging [32,33], and lifetime fluorescence tomography [34], or for noninvasive *in vivo* imaging of volumes made transparent with hydrogels [35]. The diffuse reflectance calculations can also be generalized to reconstruct the four-dimensional reflectance function for anisotropic objects [36]. Furthermore, optical mode locking and feedback might provide an alternative means for addressing spatiotemporal coding [37].

5. CONCLUSION

In conclusion, time-resolved measurements of scattered light were used in a numerical inversion algorithm to reconstruct the wide-field, spatially varying reflectance of a three-dimensional scene through a scattering layer. The method does not rely on the memory effect or coherence, but instead utilizes computational optimization techniques that are suitable for large objects. We expect this result to prove useful for new methods in image acquisition and processing of optical signals in scattering media.

ACKNOWLEDGMENTS

This work was supported by NSF grant 1115680, Charles Stark Draper grant SC001-744, and ISN grant 6927356.

REFERENCES

1. Z. Yaqoob, D. Psaltis, M. S. Feld, and C. Yang, "Optical phase conjugation for turbidity suppression in biological samples," Nat. Photonics **2**, 110–115 (2008).
2. C. L. Hsieh, Y. Pu, R. Grange, G. Laporte, and D. Psaltis, "Imaging through turbid layers by scanning the phase conjugated second harmonic radiation from a nanoparticle," Opt. Express **18**, 20723–20731 (2010).

3. X. Xu, H. Liu, and L. V. Wang, "Time-reversed ultrasonically encoded optical focusing into scattering media," Nat. Photonics **5**, 154–157 (2011).
4. Y. M. Wang, B. Judkewitz, C. A. DiMarzio, and C. Yang, "Deep-tissue focal fluorescence imaging with digitally time-reversed ultrasound-encoded light," Nat. Commun. **3**, 928 (2012).
5. K. Si, R. Fiolka, and M. Cui, "Fluorescence imaging beyond the ballistic regime by ultrasound-pulse-guided digital phase conjugation," Nat. Photonics **6**, 657–661 (2012).
6. I. Freund, "Looking through walls and around corners," Physica A **168**, 49–65 (1990).
7. S. M. Popoff, G. Lerosey, R. Carminati, M. Fink, A. C. Boccara, and S. Gigan, "Measuring the transmission matrix in optics: an approach to the study and control of light propagation in disordered media," Phys. Rev. Lett. **104**, 100601 (2010).
8. I. M. Vellekoop and A. P. Mosk, "Focusing coherent light through opaque strongly scattering media," Opt. Lett. **32**, 2309–2311 (2007).
9. S. Popoff, G. Lerosey, M. Fink, A. C. Boccara, and S. Gigan, "Image transmission through an opaque material," Nat. Commun. **1**, 81 (2010).
10. I. M. Vellekoop, A. Lagendijk, and A. P. Mosk, "Exploiting disorder for perfect focusing," Nat. Photonics **4**, 320–322 (2010).
11. F. van Beijnum, E. G. van Putten, A. Lagendijk, and A. P. Mosk, "Frequency bandwidth of light focused through turbid media," Opt. Lett. **36**, 373–375 (2011).
12. O. Katz, E. Small, and Y. Silberberg, "Looking around corners and through thin turbid layers in real time with scattered incoherent light," Nat. Photonics **6**, 549–553 (2012).
13. J. Bertolotti, E. G. van Putten, C. Blum, A. Lagendijk, W. L. Vos, and A. P. Mosk, "Non-invasive imaging through opaque scattering layers," Nature **491**, 232–234 (2012).
14. I. M. Vellekoop and C. M. Aegerter, "Scattered light fluorescence microscopy: imaging through turbid layers," Opt. Lett. **35**, 1245–1247 (2010).
15. S. Fend, C. Kane, A. Lee, and D. A. Stone, "Correlations and fluctuations of coherent wave transmission through disordered media," Phys. Rev. Lett. **61**, 834–837 (1988).
16. I. Freund, M. Rosenbluh, and S. Feng, "Memory effects in propagation of optical waves through disordered media," Phys. Rev. Lett. **61**, 2328–2331 (1988).
17. I. Freund, "Image reconstruction through multiple scattering media," Opt. Commun. **86**, 216–227 (1991).
18. G. W. Kamerman, *The Infrared and Electro-Optical System Handbook* (SPIE, 1993).
19. L. Wang, P. P. Ho, C. Liu, G. Zhang, and R. R. Alfano, "Ballistic 2-d imaging through scattering walls using an ultrafast optical Kerr gate," Science **253**, 769–771 (1991).
20. D. Huang, E. A. Swanson, C. P. Lin, J. S. Schuman, W. G. Stinson, W. Chang, M. R. Hee, T. Flotte, K. Gregory, C. A. Puliafito, and J. G. Fujimoto, "Optical coherence tomography," Science **254**, 1178–1181 (1991).
21. O. Katz, E. Small, Y. Bromberg, and Y. Silberberg, "Focusing and compression of ultrashort pulses through scattering media," Nat. Photonics **5**, 372–377 (2011).
22. D. Wu, G. Wetzstein, C. Barsi, T. Willwacher, Q. Dai, and R. Raskar, "Ultra-fast lensless computational imaging through 5D frequency analysis of time-resolved light transport," Int. J. Comput. Vis., doi: 10.1007/s11263-013-0686-0 (in press).
23. A. Velten, T. Willwacher, O. Gupta, A. Veeraraghavan, M. G. Bawendi, and R. Raskar, "Recovering three-dimensional shape around a corner using ultrafast time-of-flight imaging," Nat. Commun. **3**, 745 (2012).
24. O. Gupta, T. Willwacher, A. Velten, A. Veeraraghavan, and R. Raskar, "Reconstruction of hidden 3D shapes using diffuse reflections," Opt. Express **20**, 19096–19108 (2012).
25. P. Sen, B. Chen, G. Garg, S. R. Marschner, M. Horowitz, M. Levoy, and H. P. A. Lensch, "Dual photography," ACM Trans. Graph. **24**, 745–755 (2005).
26. J. M. Schmitt, S. H. Xiang, and K. M. Yung, "Speckle in optical coherence tomography," J. Biomed. Opt. **4**, 95–105 (1999).
27. A. Szameit, Y. Shechtman, E. Osherovich, E. Bullkich, P. Sidorenko, H. Dana, S. Steiner, E. B. Kley, S. Gazit, T. Cohen-Hyams, S. Shoham, M. Zibulevsky, I. Yavneh, Y. C. Eldar, O. Cohen, and M. Segev, "Sparsity-based single-shot subwavelength coherent diffractive imaging," Nat. Mater. **11**, 455–459 (2012).
28. S. B. Colak, D. G. Papaioannou, G. W. 't Hooft, M. B. van der Mark, H. Schomberg, J. C. J. Paasschens, J. B. M. Melissen, and N. A. A. J. van Asten, "Tomographic image reconstruction from optical projections in light-diffusing media," Appl. Opt. **36**, 180–213 (1997).
29. D. V. Dylov and J. W. Fleischer, "Nonlinear self-filtering of noisy images via dynamical stochastic resonance," Nat. Photonics **4**, 323–328 (2010).
30. E. Betzig, G. H. Patterson, R. Sougrat, O. Wolf Lindwasser, S. Olenych, J. S. Bonifacine, M. W. Davidson, J. Libbincot-Schwartz, and H. F. Hess, "Imaging intracellular fluorescent proteins at nanometer resolution," Science **313**, 1642–1645 (2006).
31. M. J. Rust, M. Bates, and X. Zhuang, "Sub-diffraction-limit imaging by stochastic optical reconstruction microscopy," Nat. Methods **3**, 793–796 (2006).
32. K. Goda, A. Ayazi, D. R. Gossett, J. Sadasivam, C. K. Lonappan, E. Sollier, A. M. Fard, S. C. Hur, J. Adam, C. Murray, C. Wang, N. Brackbill, D. Di Carlo, and B. Jalali, "High-throughput single-microparticle imaging flow analyzer," Proc. Natl. Acad. Sci. USA **109**, 11630–11635 (2012).
33. S. S. Gorthi, D. Schaak, and E. Schonbrun, "Fluorescence imaging of flowing cells using a temporally coded excitation," Opt. Express **21**, 5164–5170 (2013).
34. A. T. N. Kumar, S. B. Raymond, A. K. Dunn, B. J. Bacskai, and D. A. Boas, "A time domain fluorescence tomography system for small animal imaging," IEEE Trans. Med. Imaging **27**, 1152–1163 (2008).
35. K. Chung, J. Wallace, S.-Y. Kim, S. Kalyanasundaram, A. S. Andalman, T. J. Davidson, J. J. Mirzabekov, K. A. Zalocusky, J. Mattis, A. K. Denisin, S. Pak, H. Bernstein, C. Ramakrishnan, L. Grosenick, V. Gradinaru, and K. Deisseroth, "Structural and molecular interrogation of intact biological systems," Nature **497**, 332–337 (2013).
36. N. Naik, S. Zhao, A. Velten, R. Raskar, and K. Bala, "Single view reflectance capture using multiplexed scattering and time-of-flight imaging," ACM Trans. Graph. **30**, 171 (2011).
37. M. Nixon, O. Katz, E. Small, Y. Bromberg, A. A. Friesem, Y. Silberberg, and N. Davidson, "Real-time wavefront shaping through scattering media by all-optical feedback," Nat. Photonics **7**, 919–924 (2013).